Interpretation®

Geophysical properties of an epithermal Au-Ag deposit in British Columbia, Canada

Journal:	*Interpretation*
Manuscript ID	INT-2017-0232.R1
Manuscript Type:	Technical Paper (if no special section applies)
Date Submitted by the Author:	27-Jun-2018

Complete List of Authors:	Abbassi, Bahman; Université du Québec en Abitibi-Témiscamingue, Institut de recherche en mines et en environnement (IRME) Cheng, Li Zhen; Uniersity of Quebec in Abitibi Temiscamingue, Applied Sciences Richards, Jeremy; University of Alberta, Department of Earth and Atmospheric Sciences Edmonton; Laurentian University, Harquail School of Earth Sciences Hübert, Juliane; The University of Edinburgh, School of Geosciences; University of Alberta, Department of Earth and Atmospheric Sciences Legault, Jean; Geotech Ltd., Data Processing & Interpretation Rebagliati, Mark; Amarc Resources Ltd., Witherly, Ken; Condor Consulting,

Keywords:	3D, electrical/resistivity, induced polarization (IP), magnetic susceptibility, radiometrics
Subject Areas:	Case studies, Application examples (applying a relatively new technique or concept)

GEOPHYSICAL PROPERTIES OF AN EPITHERMAL AU-AG DEPOSIT IN BRITISH COLUMBIA, CANADA

Authors:

1. Bahman Abbassi: Ph.D. Student, Université du Québec en Abitibi-Témiscamingue (UQAT), Québec, Canada. bahman.abbassi@uqat.ca
2. Li Zhen Cheng: Professor, Université du Québec en Abitibi-Témiscamingue (UQAT), Québec, Canada. Li_Zhen.Cheng@uqat.ca
3. Jeremy P. Richards: Professor, Harquail School of Earth Sciences, Laurentian University, Sudbury, Canada. JRichards2@laurentian.ca
4. Juliane Hübert: Postdoctoral Research Associate, School of Geosciences, University of Edinburgh, Edinburgh, UK. juliane.huebert@ed.ac.uk
5. Jean M. Legault: Chief Geophysicist, Geotech Ltd., Aurora, Ontario, Canada. jean@geotech.ca
6. Mark Rebagliati, Executive Vice President, Amarc Resources Ltd., Vancouver, Canada. markrebagliati@hdimining.com
7. Ken Witherly: President, Condor Consulting, Inc., Lakewood CO, USA. ken@condorconsult.com

Original paper date of submission: ----

Revised paper date of submission: ----

ABSTRACT

The Newton Au-Ag deposit is an intermediate sulfidation state epithermal system in British Columbia, Canada. Multiple types of geophysical data are interpreted and evaluated with drillcore petrophysical, geochemical and geological observations to better understand the geophysical signature of the Newton epithermal system. Airborne γ-ray datasets show elevated emission counts of K, eTh, and eU over the Newton epithermal system that are caused by hydrothermal alteration. Drillcore γ-ray measurements also show high potassium concentrations related to the K-rich phyllosilicates in the form of argillic and quartz-sericite alteration assemblages. Magnetization vector inversion (MVI) is used to recover an unconstrained 3D magnetization vector model of the system on regional and deposit scales. The regional MVI has resolved a deep concentric shaped low magnetic zone that is interpreted as a porphyry system beneath the epithermal deposit. At the deposit scale, 3D direct current (DC) resistivity and induced polarization (IP) inversion, and unconstrained MVI revealed finer details of epithermal system architecture. Cooperative DC/IP and magnetic inversion, at the deposit scale, constrained the magnetic susceptibility model and recovered a more precise susceptibility image of the epithermal system that is well-matched with borehole geology. The integrated geophysical interpretation helped to resolve several 3D latent geological features in places without direct access to drillcore samples. We identified four petrophysical domains based on the three cooperatively inverted physical properties, including electrical resistivity, IP chargeability, and magnetic susceptibility. The combined geophysical models differentiated porphyritic intrusions (chargeability/susceptibility lows), disseminated sulfides (resistivity lows and chargeability highs), a Cu-rich zone in mafic volcanic rocks (susceptibility/chargeability highs and resistivity lows), and a Au-Ag-Cu-rich zone with silicification in felsic volcanic rocks

(chargeability/susceptibility lows and resistivity highs). These petrophysical domains also provide useful exploration vectors for identification of similar epithermal systems.

INTRODUCTION

Shallow (< 1.5 km) hydrothermal deposits formed at depths below boiling hot springs (< 300 °C) are commonly referred to as epithermal deposits (Simmons et al., 2005; Pirajno, 2009). The Newton epithermal system consists of hydrothermal disseminations of gold (Au) and silver (Ag) as inclusions in pyrite with variable amounts of copper (Cu) mineralization in British Columbia, Canada (Figure 1). Based on sulfide mineral assemblages, the Newton epithermal deposit is characterized as an intermediate sulfidation type in which sulfur and oxygen fugacities are gradational between low sulfidation and high sulfidation regime (Pressacco, 2012; McClenaghan, 2013). The epithermal system is hidden within a very complex geological framework under quaternary sediments and vegetations (Pressacco, 2012; McClenaghan, 2013). In this study, we present a 3D integrated geophysical model of the Newton epithermal deposit that reconciles all geophysical, petrophysical and geological observations from regional to deposit scale.

Similar epithermal types of mineralization around the world are commonly accompanied either by (1) quartz veins, or (2) disseminated sulfides, which cause significant contrasts in physical properties between the mineralization and the background rocks (Allis, 1990; Irvine and Smith, 1990; Feebreyf et al., 1998; Murakami, 2008; Morrell et al., 2011; Clark, 2014; Hübert et al., 2016; Legault et al., 2016). Relatively cool CO_2-bearing hydrothermal fluids in epithermal systems usually destroy magnetite and cause demagnetization anomalies (Allis, 1990; Murakami, 2008; Clark, 2014). The late-stage volcanic flows post-dating the epithermal mineralization may

obscure the deeper demagnetization zones (Allis, 1990), and in some cases, like on Olkaria system in the rift valleys of Kenya, the demagnetization extends to 4 km depth (Allis, 1990). Electrical resistivity-highs (locally exceeding 1000 Ohm-m) are associated with silicification, compaction, and intermediate-to-felsic intrusions (Allis, 1990). Low resistivities from sulfidation (3-30 Ohm-m; Allis, 1990), which are most favorable to hydrothermal exploration, are often mixed with resistivity-lows of pore fluid and pervasive clay alteration (Nelson and Van Voorhis, 1983; Allis, 1990; Irvine and Smith, 1990). Strong IP chargeabilities due to the hydrothermal alteration are typically associated with the presence of disseminated sulfidation (Sumner, 1976; Allis, 1990). Alteration haloes over epithermal Au-Ag deposits are also detected through γ-ray surveys by Irvine and Smith (1990); Feebrey et al. (1998) and Morrell et al., (2011). Radiometric data from the Waihi-Waitekauri epithermal Au-Ag deposit in New Zealand shows widespread potassium enrichment related to K-rich phyllosilicates in the core of the epithermal system (Morrell et al., 2011).

Exploration activities in the Newton area have been conducted since the 1970s, and comprise geological, geochemical and geophysical surveys (Pressacco, 2012). The most recent study (Hübert et al., 2016) has modeled regional electrical resistivity structure of the Newton deposit using magnetotelluric (MT) and airborne z-axis tipper electromagnetic (ZTEM) data. The area of hydrothermal mineralization exhibits a modest electrical response relative to the country rocks, mainly due to the presence of phyllosilicate minerals (sericite) and minor epithermal sulfides (Hübert et al., 2016). However, the ZTEM-MT resistivities do not possess the resolution of the deposit scale electrical features.

In this study, results of multiple geophysical measurements and inversions are presented in two subsequent scales over the Newton deposit to increase the understanding of the Newton epithermal system. We provide an example of 3D integration of geological, petrophysical and geophysical models in order to image the 3D volume of the hydrothermal system from near surface to 5 km depth. The 3D integration unveiled specific physical property patterns related to the host geology and epithermal mineralization that can be used as exploration vectors for identification of similar petrophysical domains in epithermal systems.

GEOLOGICAL SETTING

Regional geology

Radiometric dating of molybdenite within the Newton epithermal Au-Ag deposit yielded an age of 72.1 ± 0.3 Ma (McClenaghan, 2013) in association with Late Cretaceous arc magmatism in the accreted Stikinia terrane of western Canada (Figure 1). Amarc Resources Ltd. acquired the property in 2009, and after an extensive drilling campaign defined an estimated inferred mineral resource of 111.5 Mt with an average grade of 0.44 g/t Au (cut-off at 0.25 g/t Au; Pressacco 2012).

Regionally (Figure 2), the Late Cretaceous volcanic sequence is overlain by Miocene-Pliocene Chilcotin Group flood basalts, and Quaternary glacial deposits, which are variably eroded to expose the older rocks. The epithermal mineralization associated with the Newton deposit is at a depth of ~50 m to ~600 m. The mineralization is characterized by pervasive sericitic (phyllic) alteration containing disseminated pyrite with Au inclusions in coeval intermediate composition porphyritic volcanic and subvolcanic intrusive rocks. Au-Ag

mineralization is mainly associated with disseminated pyrite, marcasite, and base metal sulfides (McClenaghan, 2013; Liu et al., 2015).

Deposit scale bedrock geology

Quaternary glacial tills cover most of the Newton property. Consequently, deposit scale geological information has primarily been obtained from drill cores (Pressacco, 2012). A bedrock geology map of the property is compiled from the mapping of limited outcrops, drill cores and cross-section interpretations (Figure 3). Three volcano-sedimentary sequences overlain on each other from bottom to top are mafic volcanic rocks, sedimentary rocks and felsic volcanic rocks (72.1±0.6 Ma; McClenaghan, 2013). These layered rocks are intruded by intermediate-to-felsic porphyritic intrusions, including the monzonite (72.1±0.3 Ma; McClenaghan, 2013), quartz feldspar porphyry (QFP; 70.9±0.5 Ma; McClenaghan, 2013), feldspar biotite porphyry (FBP) and diorite (69.3±0.4 Ma; Liu et al., 2015).

BOREHOLE GEOLOGY AND PETROPHYSICS

3D lithology and hydrothermal alteration model

Based on a database of 130 boreholes comprising a total of 1537 drillcore samples (Amarc written communications; Pressacco, 2012), a 3D lithological model is constructed for the Newton property. A cross-section of the 3D model is shown in Figure 4a. As can be seen, the laterally discontinuous volcanic sequences are intruded by several phases of intermediate-to-felsic intrusions. The deposit is offset by the Newton Hill Fault (NHF), which displaces the geology and mineralization by ~300 m of normal dip-slip movement.

Based on the geochemical assessment from the database of Amarc and previous works of McClenaghan (2013) and Liu et al. (2015), a 3D model of hydrothermal alteration is also generated. The cross-sections of the 3D models (Figure 4a and 4b) show the highest gold contents occur mainly within the felsic volcanic sequence and in association with quartz-sericite-pyrite alteration. Propylitic alteration comprising chlorite-epidote-pyrite-calcite-albite-magnetite assemblage occurs mostly in the mafic volcanic rocks and epiclastic sedimentary units (Pressacco, 2012; McClenaghan, 2013). Minor potassic alteration, characterized by secondary biotite and minor pyrite, occurs in the diorite intrusion (Liu et al., 2015). Silicification and albitic alteration are spatially associated and are interpreted to comprise a single quartz-albite assemblage. The quartz-albite assemblage is mostly seen in QFP intrusions (Pressacco, 2012; McClenaghan, 2013). Localized argillic alteration (kaolinite-sericite-calcite) is of late stage or surficial (supergene) origin.

The Au-Ag mineralization is mainly hosted within the felsic volcanic sequence and coeval intermediate-to-felsic intrusions (monzonites, FBP and QFP). The first stage of gold mineralization with disseminated pyrite-arsenopyrite is strongly associated with a pervasive quartz-sericite alteration (Pressacco, 2012; McClenaghan, 2013). Later, the gold mineralization is associated with a quartz-sericite-marcasite alteration (McClenaghan, 2013; Liu et al., 2015). The latest stage of mineralization consists of polymetallic sulfide veins containing pyrite, chalcopyrite, arsenopyrite, and sphalerite, but lack gold enrichment (Liu et al., 2015).

Drillcores magnetic susceptibility and γ-ray radioelement concentrations

More than 9000 magnetic susceptibility readings from core samples from 80 drillholes in the Newton Hill area are available. Samples are measured by KT-10 S/C meter of Terraplus Inc.

and are supported by additional susceptibility data provided by Amarc (Figure 5). The γ-ray spectra of 12 borehole samples (514 drillcores) are also measured using Radiation Solutions RS-125 that measures γ-ray emission counts in 1024 energy windows.

To establish a direct link between the magnetic susceptibilities, γ-ray concentrations, and the geology, the measured properties are classified according to lithological types and accompanying alteration assemblages. A 3D nearest-neighbor interpolation (Trauth, 2015) is used to regularize all data sets. The nearest-neighbor operation assigns susceptibility/ γ-ray K values or lithology/alteration codes to nearest cells in the vicinity of the available data points. The advantage of this approach is that the statistical range (minimum, maximum) of the original susceptibility measurements remain intact. However, a number of outlier samples resulted in apparently wide ranges of susceptibility/K variations (wide statistical dispersion). Therefore, a better way to rank rocks' properties is to look for the inter-quartile ranges of the data values (the interval between 25^{th} and 75^{th} percentiles). The retrieved statistics of measured magnetic susceptibilities and potassium radionuclide concentration of different lithologies and alteration assemblages are shown as box plots in Figure 6a and 6b.

The drillcore susceptibility measurements illustrate that there are diverse geological sources giving rise to the observed magnetic-highs. Listed from oldest to youngest, the magnetic-high sources are mafic volcanic rocks, potassic/propylitic alteration assemblages, and dioritic intrusions (Figure 6a). The high amplitude susceptibility anomaly (exceeding than ~ 0.001 SI) is likely due to a blend of mafic volcanic rocks, overprinted by magnetite-bearing alteration and the later emplaced dioritic intrusion. Critically, low susceptibility sources are limited to porphyritic

intrusions and the felsic volcanic rocks overprinted by quartz-sericite alteration in the Au mineralization zone (Figure 6a).

Concentrations of all three γ-ray radioelements including potassium (K), equivalent thorium (eTh) and equivalent uranium (eU) increase over the Newton epithermal system. The distribution of γ-ray potassium is disperse in all lithologies due to severe chemical alteration (Figure 6b). The low magnetic rocks (proximal to Au-rich zone) are accompanied by high concentrations of γ-ray potassium. This is likely due to the presence of potassium-rich phyllosilicates in the form of argillic and quartz-sericite alteration assemblages in the low-magnetic epithermal mineralization zone.

REMOTELY SENSED GEOPHYSICAL DATA

Geotech Ltd. has acquired the aeromagnetic data as a part of the combined magnetic and ZTEM survey, carried out between January to February 2010, on behalf of Amarc (Geotech Ltd, 2010). The ZTEM datasets are described in Hübert et al. (2016). Total magnetic field intensity data were measured from a helicopter flown at a mean height of 155 m above ground. The data were collected along N–S flight lines at 200 m spacing and E–W tie lines flown every ~2000 m to 500 m (tighter spacing near the deposit). A total of 7071 line-km of data were collected and cover a 1293 km^2 area. The magnetometer sampling rate was 0.1 second and depending on the speed of the helicopter results in approximately 10 m measurement intervals along each profile.

A previous airborne magnetic survey that covers an area of ~1100 km^2, was flown in July 1993 by Geological Survey of Canada (GSC; Shives et al., 1995), using a fixed-wing aircraft at a mean height of 120 m above the ground, with E-W lines spaced ~500 m apart, provides a

regional context and are used to better characterize longer wavelengths related to the deeper magnetic sources beneath the epithermal system. The measured magnetic datasets of GSC and Amarc are shown in Figure 7.

The GSC dataset also contains airborne γ-ray measurements in the form of K-eTh-eU radionuclide concentrations. In the Figure 8a, the absolute values of radionuclide concentrations are displayed as red (K), green (Th) and blue (U). Figure 8b also present the ratios of radionuclide elements in form of ternary red (K/eTh), green (eTh/eU) and blue (eU/K) images.

A DC/IP survey of 85 line-km over Newton Hill area, using the "pole-dipole" electrode configuration was conducted in 2010 (Pressacco, 2012). The survey lines were spaced at 200 m intervals in E–W directions within the zone of hydrothermal alteration (Figure 7b). The dipole length was set to 100 m and 200 m, with a maximum ten times dipolar separations. The apparent chargeabilities (in mV/V) were measured by recording the decaying voltage after the current cut-off.

METHODS

γ-ray data interpretation

Investigation of all ratios and combination of K, eTh, and eU is a useful tool to detect the anomalous hydrothermal zones. A ternary image combination is used to produce RGB (red-green-blue) images of the radionuclides and their ratios. When all three radionuclides are abundant, the display tends towards white; otherwise, it tends towards black (Dentith and Mudge, 2014). In this study, the three radiometric channels (K, eTh, and eU) are normalized, and their histograms are equalized for enhanced RGB visualization (Figure 8).

3D unconstrained magnetization vector inversion

Igneous rocks of the Newton Hill area have experienced a complicated geological history, including different phases of magmatism, hydrothermal alteration, and tectonic disruptions from the late Cretaceous to Pliocene (Pressacco, 2012; McClenaghan, 2013; Liu et al., 2015). To consider the effect of the magnetic remanence in the Newton area, an accurate approximation proposes a vector notion of magnetic response (total magnetization vector) as a vector summation of two vector components, including the inductive magnetization vector ($\vec{J}_{Ind}$) and a remanent magnetization vector ($\vec{J}_{\mathrm{Re}m}$). Moreover, the total susceptibility of rocks in the presence of remanence will be a function of (Lelièvre and Oldenburg, 2009; Ellis et al., 2012):

$$\chi_{Total} = \left|\vec{J}_{Total}\right| / \left|\vec{H}_0\right| = \left|\vec{J}_{Ind} + \vec{J}_{\mathrm{Re}m}\right| / \left|\vec{H}_0\right| \qquad (1)$$

A 3D magnetization vector inversion (MVI) is executed on the regional and deposit scales. The cell dimensions of the inversion model at the regional scale are 100 m (in X-direction), 100 m (in Y-direction) and 20 m (in Z-direction) that comprise total 2646000 cells. In the deposit scale, the cell dimensions of the inversion model are 25 m (in X-direction), 25 m (in Y-direction) and 10 m (in Z-direction) that comprise total 3148308 cells, covering the hydrothermal zone.

The MVI algorithm introduces both the amplitude and the vector direction as separate unknowns in a Tikhonov minimum gradient regularization (Lelièvre and Oldenburg, 2009; Ellis et al., 2012). An Iterative Reweighting Inversion (IRI; Geosoft Inc., 2012) method is used in parallel to the MVI modeling in this study. Iterative Reweighting Inversion tends to recover

sharp magnetic variations, and its results are equivalent to Robust or Blocky Inversion in inverse modeling of electrical resistivity data (Claerbout, 1973; Loke et al., 2003).

3D DC/IP inversion

A 3D cooperative inversion algorithm (Loke, 2015) is employed using a modified L_1-norm optimization to produce sharpened resistivity and chargeability images. Electrodes distributed initially on each node in 50 by 18 horizontal grids in X and Y direction respectively. For more accurate calculations, each cell is divided into two parts toward East and North directions so that instead of a single cell, two cells covered the space between two adjacent electrodes in each EW-NS direction. Therefore, each cell has a 50 m by 100 m size in a horizontal plane, and they shape a large model mesh consisting of 72000 trapezoidal cells.

The DC/IP inversion considers the IP chargeability model as a small perturbation of the reference electrical conductivity model (Oldenburg and Li 1994; Li and Oldenburg, 2000). The program calculates the forward potential responses of two conductivity models separately. The forward modeling of the reference and perturbed conductivities gives the reference and perturbed potential values, from which the apparent conductivities and chargeabilities are obtainable. In each iteration, an Incomplete Gauss-Newton least-squares optimization tries to reduce the gap between measured and calculated properties by modifying the reference and perturbed conductivity values. When the calculation reaches its threshold, i.e., the relative change in the error between two subsequent iterations (5 percent in this study), the modeled resistivities and chargeabilities are determined respectively.

The robust inversion in this study, which uses an extension of L_2-norm and L_1-norm inversions (Loke et al., 2003), incorporates two cut-off factors in the resistivity-chargeability inversion (k_1 and k_2). Larger k_1 values produce smoother apparent resistivities and chargeabilities. The second cut-off factor (k_2) shapes the modeled resistivity and chargeability outputs. The larger k_2, the smoother the predicted resistivity and chargeability values.

3D cooperative magnetic-DC/IP resistivity inversion

Without any constraint, the inversion of magnetic data is vulnerable to the lack of depth estimation accuracy. One way to reduce the MVI uncertainty is to provide auxiliary information about the susceptibility distribution from other geophysical methods. Since the sulfide mineralization in the area is dominantly occurred in the Cretaceous volcanic sequences, comprising interbeds of mafic rocks with a minor amount of felsic and sedimentary rocks, we expected an underlying relationship between the magnetic susceptibility of volcanic sources and IP chargeability of sulfide disseminations. Therefore, the results of the DC/IP inversion were used to constrain the subsequent magnetic susceptibility inversion. It was noticed that when the magnetization vectors of the MVI were rotated to the present geomagnetic field direction, the magnetic response of the rotated model is very similar to the magnetic response of the IP-driven susceptibilities (Abbassi et al., 2017). Considering this underlying connection between the 3D magnetic susceptibility and IP chargeability models, the conventional susceptibility inversion (Li and Oldenburg, 1997) is constrained by the initial susceptibility information derived from IP chargeabilities.

In the cooperative inversion, four nodes between adjacent electrodes are used, so that the number of cells in the forward calculations has effectively increased to 288000 cells, and each

cell, therefore, has a 25 m by 50 m size in the horizontal plane. The unit cell size for the cooperative susceptibilities inversion is set to X = 25 m, Y = 25, and Z = 10 m, with a total number of 613800 cells, covering a smaller area limited to the mineralization zone (the area covered by boreholes). The constrained inversion set aside the less consistent equivalent solutions and narrowed down to a final solution that is well matched with the DC/IP inversion results.

RESULTS

The interpretation results are presented as 3D physical property distributions, including 3D electrical resistivities (ρ), IP chargeabilities (m) and magnetic susceptibilities (χ), in the three following sections:

Regional unconstrained interpretation

Unconstrained MVI recovered susceptibility distributions down to 5km using the GSC dataset, which helped to predict the regional magnetic field trend in the subsequent deposit scale MVI. A deep high susceptibility zone with distinct magnetization vector orientation is derived from this inversion (Figure 9). As can be seen in the cross-section A-A', the high susceptibility zone has a very deep root down to at least 3 km below sea level and encompasses a low magnetic zone (LMZ) within itself, with different magnetization vector orientations. The concentric shape of this LMZ might imply a hydrothermal alteration pattern related to a deeper porphyry system.

Deposit scale unconstrained interpretation

High radionuclide concentrations caused by phyllosilicates in the hydrothermal alteration zone (white zones in Figure 8a) are associated with bedrock exposures over Newton epithermal system. The RGB demonstration of radioelements ratios provides a better way to differentiate anomalies and shows a northwest-southeast trend over porphyritic intrusions and volcanic rocks (Figure 8d).

Unconstrained MVI and DC/IP inversions reveal finer patterns over the area of the hydrothermal alterations. The MVI results are shown in Figure 10. The Au-Ag-Cu-rich zone appears in a near-surface low magnetic zone. The geological context is better seen from the section view (Figure 10c), where low magnetic susceptibilities indicate rocks on the eastern side of NHF, and igneous rocks in the west of the Newton Hill fault correspond to relatively high magnetization (Figure 10c). The cross-section shows the likely occurrence of mafic volcanic strata overlying a deep LMZ, though the relatively thick layer of top magnetic rocks in the unconstrained inversion (Figure 9b) is not in good agreement with available petrophysical information (Figure 5).

The results of 3D deposit scale inversion of DC/IP data are illustrated in Figure 11 and Figure 12. The preliminary 2D inversions proved that the main electrical anomaly is elongated sub-vertically. However, regional geological observations show that the Cretaceous volcanic rocks and the related intrusive rocks are mostly horizontally layered. Therefore, performing smoothness horizontally could uncover the hidden anomaly sources. This is done by decreasing the vertical to horizontal flatness filter ratio (R_f). In this study, the most stable results came out with the $R_f = 0.2$.

DC/IP inversion is controlled by different k_1 and k_2 factors to see which output is more consistent with our prior knowledge of the region. Getting too close to the L_2-norm criteria (larger cut-off factors) increased the misfit error. Closer to L_1-norm (smaller cut-off factors) produced too sharp boundaries not consistent with magnetic inversion and prior geological information. The most consistent results obtained with $k_1 = 0.05$ and $k_2 = 0.01$.

A significant low resistivity zone with an NW-SE trend is hidden under a large resistivity cap (Figure 11). The electrical resistivity image differentiated a very resistive mafic volcano-sedimentary mixture from a low-resistivity region related to a mix of porphyritic intrusions, felsic volcanic rocks, and the younger dioritic intrusion. Therefore, the host rock of Au mineralization (sericite altered felsic volcanic rocks) is distinguished by a low-resistivity body, though in some places, other low-resistivity sources (within the dioritic and porphyritic intrusions) contribute to the bulk resistivity-lows.

The chargeability of sulfide dissemination (Figure 12) is more than 50 mV/V, and is related to 2-7% disseminated sulfide mineralization, comprising pyrite, marcasite, sphalerite, chalcopyrite, and arsenopyrite (McClenaghan, 2013; Liu et al., 2015). Minor chargeability contributors are probably clay contents and membrane polarizations in fracture zones and hydrothermal alterations.

Deposit scale constrained interpretation

At this scale (the area covered by boreholes), the cooperative DC/IP and magnetic inversion is focused further to the epithermal mineralization zone. The result of the cooperative magnetic-DC/IP inversion is also shown in Figure 13. No prior geological information has been

used to constrain the inversion. Yet, the cooperative inversion results are reasonably matched with the known borehole geology. As can be seen, the porphyritic intrusions at the center of deposit show low amplitude susceptibilities that are surrounded by a ring of high magnetic mafic volcanic rocks. The diorite intrusion is also imaged as a large magnetic-high in the northwest. By comparing Figure 13c and Figure 10b, it is evident that constraining the magnetic inversion with IP chargeability model has produced a more precise magnetic susceptibility image that is in good agreement with observed geology.

The cooperatively inverted physical properties are classified into several distinct petrophysical domains on a series of cross-plots (Figure 14). Physical property cross plots for every pair of physical properties are divided into separate regions based on the lower (20^{th}, blue color) and higher (80^{th}, orange color) percentiles of the third physical property. Four distinct petrophysical domains (Table 1) are inferred from the integration of physical properties on the three physical properties' cross-plots.

In Figure 15, the cooperative inversion results are compared with borehole information on cross sections (see profile AA' in Figures 3, 4 and 5). The results predict the continuation of the hidden features to deeper levels (Figure 15d). The high magnetic cap is thinner in the constrained inversion, as can be seen in Figures 15c and 15d, and is related to a mixture of the mafic volcanic rocks (MV) and the younger dioritic intrusions (D). Though, the LMZ was positioned deeper in earlier unconstrained modeling (Figures 9 and 10), the cooperative inversion has resolved it about 500 m higher elevation and directly beneath the high magnetic cap (magnetic susceptibilities > 0.04 SI). Several flanks of this LMZ locally reduce the magnetic susceptibilities to 0.015 SI inside the high magnetic cap. This structure is interpreted as a

response of intermediate-to-felsic porphyritic intrusions (FIP) and interbeds of felsic volcanic rocks (FV) within the upper high magnetic cap (Domain 1 and FIP in Figures 15c and 15d). Note that the Domain 1 repeats on both cross-plots of Figures 14a and 14c.

Pyrite is the dominant disseminated sulfide and is accompanied by high chargeabilities and low resistivities (Domain 2). The northwest part of the mineralization (within the gray shaded regions in Figure 13) is exclusively a Cu-rich zone with high magnetic susceptibilities, high chargeabilities and low resistivities due to the presence of more magnetite-bearing rocks and sulfides (Domain 3). The quartz-sericite assemblage is accompanied by Au-Ag-Cu mineralization on the hanging wall of NHF and appears as a silicified Au-Ag-Cu-rich zone with high resistivity and low chargeability/susceptibility (Domain 4).

CONCLUSION

The geophysical data processing and interpretation presented above successfully identifies several geological features, at disparate scale, related to the epithermal Au system at Newton. There is a diverse source of geophysical anomalies, however, that collectively mix to contribute to the observed geophysical signals. At the regional scale, MVI revealed a high susceptibility zone with a very deep root that contains a LMZ within itself. The concentric shape of this LMZ might imply a hydrothermal alteration pattern related to a deep underlying porphyry system. Several flanks of the LMZ reach the surface that are related to the felsic to intermediate porphyritic intrusions near a shallow post mineralization thrust fault.

DC/IP inversion uncovered a significant low resistivity zone under a large resistivity cap. The host rock of Au mineralization (quartz-sericite altered felsic volcanic rocks) in resistivity

image manifests as a low-resistivity body, though in some places, other low-resistivity sources (i.e., within the dioritic and porphyritic intrusions) participate in the bulk resistivity-lows. The chargeability-highs are related to the distribution of pyrite, marcasite, sphalerite, chalcopyrite, and arsenopyrite.

The cooperative magnetic-DC/IP inversion reduced the magnetic inversion uncertainty at the deposit scale and provided an enhanced magnetic susceptibility image of the deposit. The constrained magnetic susceptibility model detects the highly magnetic mafic volcanic rocks and diorites, as well as susceptibility-lows of the porphyritic intrusions and felsic volcanic rocks (host rock of Au). In some places, there is still ambiguity in the distinction between magnetic-highs of diorite and mafic volcanic rocks, as well as susceptibility-lows of felsic volcanic rocks (host rock of Au) and porphyritic intrusions.

The 3D integrated interpretations in this study, distinguish distinct physical property patterns related to the host geology and epithermal mineralization. These patterns are useful exploration vectors for identification of similar petrophysical domains in epithermal systems. Four petrophysical domains are inferred from cross-correlation of physical properties, including:

- Domain 1: A low chargeability and low susceptibility zone related to the porphyritic intrusions with variable resistivity values.
- Domain 2: A low resistivity and high chargeability zone with variable susceptibility values related to the sulfide dissemination.
- Domain 3: A Cu-rich zone with high susceptibilities and chargeabilities and low resistivities due to the presence of more magnetite-bearing rocks and sulfides.

- Domain 4: A Au-Ag-Cu-rich zone with low susceptibilities, low chargeabilities and high resistivities (silicifications).

Further studies in development include the application of multivariate feature extraction and machine learning to uncover the hidden patterns inside the multiple images semi-automatically.

ACKNOWLEDGEMENTS

This work is funded by a Strategic Projects Grant from the Natural Sciences and Engineering Research Council of Canada with industry partners Amarc Resources Ltd., Geotech Ltd., Gerald G. Carlson, and John A. Chapman. Amarc Resources Ltd. is particularly thanked for providing access to drillcore and geophysical data; Geotech Ltd. is acknowledged for the collection of the aeromagnetic data as well valuable discussions with us through the project. We also thank Walcott Geoscience for collecting DC/IP data and in-field assistance.

REFERENCES

Allis, R.G., 1990, Geophysical anomalies over epithermal systems: Journal of Geochemical Exploration, **36**, 339-374.

Claerbout, J.F. and F. Muir, 1973, Robust modeling with erratic data: Geophysics, **38**, 826-844.

Clark, D.A., 2014, Magnetic effects of hydrothermal alteration in porphyry copper and iron-oxide copper-gold systems: A review: Tectonophysics, **624 & 625**, 46-65.

Dentith, M., and S. T. Mudge, 2014, Geophysics for the Mineral Exploration Geoscientist: Cambridge University Press.

Ellis, R. G., B. de Wet, I. N. MacLeod, 2012, Inversion of magnetic data for remanent and induced sources: 22th International Geophysical Conference and Exhibition, ASEG, Extended Abstracts, 1-4.

Feebreyf, A.F., H. Hishida, K. Yoshioka, and K. Nakayama, 1998, Geophysical Expression of Low Sulphidation Epithermal, Au-Ag Deposits and Exploration Implications – Examples from the Hokusatsu Region of SW Kyushu, Japan: Resource Geology, **48**, 75-86.

Geosoft Inc., 2012, Sharpening using Iterative Reweighting Inversion: Oasis Montaj Best Practice Guide, Geosoft Inc. http://updates.geosoft.com/downloads/files/how-to-guides/Best-Practice-Guide_Sharpening_using_IRI.pdf

Geotech Ltd., 2010, Report on a helicopter-borne Z-axis tipper electromagnetic (ZTEM) and aeromagnetic geophysical survey: Technical Report, Geotech Ltd., Canada, Projects 10005, 10010 and 10016.

Geotech Ltd., 2010, Report on a helicopter-borne Z-axis tipper electromagnetic (ZTEM) and aeromagnetic geophysical survey: Technical Report, Geotech Ltd., Canada, Projects 10005, 10010 and 10016.

Hübert, J., B.M. Lee, L. Liu, M. J. Unsworth, J. P. Richards, B. Abbassi, L.Z. Cheng, D.W. Oldenburg, J. M. Legault, and M. Rebagliati, 2015, Three-dimensional imaging of a Ag-

Au-rich epithermal system in British Columbia, Canada, using airborne z-axis tipper electromagnetic and ground-based magnetotelluric data: Geophysics, **81**, B1-B12.

Irvine, R.J., and M.J. Smith, 1990, Geophysical Exploration for Epithermal Gold Deposits: Journal of Geochemical Exploration, **36**, 375-412

Legault, J.M., J., Niemi, J.S., Brett, S., Zhao, Z., Han, and G.C., Plastow, 2016, Passive Airborne EM and ground IP\resistivity results over the Romero intermediate sulfidation epithermal gold deposits, Dominican Republic: Exploration Geophysics, 47(3), 191-200.

Lelièvre P.G. and D.W. Oldenburg, 2009, A 3D total magnetization inversion applicable when significant, complicated remanence is present: Geophysics, **74**, L21–L30.

Li, Y., and D.W. Oldenburg, 1997, 3D inversion of magnetic data: Geophysics, **61**, 394-408.

Li, Y., and D. W. Oldenburg, 2000, 3D inversion of induced polarization data: Geophysics, **65**, 1931-1945.

Liu, L., J. P. Richards, A. DuFrane, and M. Rebagliati, 2015, Geochemistry, geochronology, and fluid inclusion study of the Late Cretaceous Newton epithermal gold deposit, British Columbia: Canadian Journal of Earth Sciences, **53**, 10-33.

Loke, M.H., 2015, Tutorial: 2D and 3D electrical imaging surveys: Geotomo Software. http://www.geotomosoft.com/downloads.php.

Loke, M.H., I., Acworth, and T., Dahlin, 2003, A comparison of smooth and blocky inversion methods in 2D electrical imaging surveys: Exploration Geophysics, **34**, 182-187.

Massey, N.W.D., D.G. MacIntyre, P.J. Desjardins, and R.T. Cooney, 2005, Digital Geology Map of British Columbia: B.C. Ministry of Energy and Mines, Open File 2005-2, DVD.

McClenaghan, L., 2013, Geology and genesis of the Newton bulk-tonnage gold-silver deposit, central British Columbia: M.S. thesis, University of British Columbia.

Morrell, A.E., C.A. Locke, J., Cassidy and J., Mauk, 2011, Geophysical characteristics of adularia-sericite epithermal gold-silver deposits in the Waihi-Waitekauri region, New Zealand: Economic Geology, **106**, 1031–1041.

Murakami, H., 2008, Variations in Chemical Composition of Clay Minerals and Magnetic Susceptibility of Hydrothermally Altered Rocks in the Hishikari Epithermal Gold Deposit, SW Kyushu, Japan: Resource Geology, **58 (1)**, 1-24.

Nelson, P.H., and G.D. Van Voorhis, 1983, Estimation of sulfide content from induced polarization data: Geophysics, **48**, 62–75.

Oldenburg, D.W., and Y. Li, 1994, Inversion of induced polarization data: Geophysics, **59**, 1327-1341.

Pirajno, F., 2009, Hydrothermal Processes and Mineral Systems: Springer.

Pressacco, R., 2012, Initial resource estimate for the Newton project, central British Columbia, Canada: Technical Report, NI43-101.

Shives, R.B.K., P.B., Holman and L. Rebolledo, 1995, Airborne geophysical survey, Fish Lake, British Columbia (Open File 2800): Geological Survey of Canada, 82p. http://www.empr.gov.bc.ca/MINING/GEOSCIENCE/PUBLICATIONSCATALOGUE/OPENFILES/2005/Pages/2005-10.aspx

Simmons, S.F., N.C., White., D. A., John, 2005, Geological characteristics of epithermal precious and base metal deposits. In: Hedenquist, J.W., Thompson, J.F.H., Goldfarb, R.J., Richards, J.P. (Eds.), 100th Anniversary Volume: Economic Geology, Society of Economic Geologists, 485-522.

Sumner, J. S., 1976, Principles of induced polarization for geophysical prospecting: Elsevier.

Trauth, M.H., 2015, MATLAB® Recipes for Earth Sciences: Fourth Edition: Springer.

LIST OF FIGURES

Figure 1. Several large porphyry and epithermal deposits located in Stikinia terrain (ST) in central British Columbia. Other terranes are: AX Alexander terrane; BR Bridge River terrane; CAC Caribo terrane; CC Cache Creek terrane; CD Cadwallader terrane; CX Coast Complex terrane; HA Harrison terrane; KO Kootenay Terrane; MO Monashee; NA Cratonal North America terrane; NI Nisling terrane; PAP Post Accretionary Plutons; QN Quesnellia terrane; SH Shuksan terrane; SM Slide Mountain Terrane; WR Wrangellia (Modified from Massey et al., 2005).

Figure 2. Regional geological features of Newton area, modified after British Columbia Geological Survey Geoscience Map (mapplace.ca). Geology is draped on shaded relief topography.

Figure 3. Bedrock geology map at the deposit scale. Colored dots indicate drillhole locations with various total lengths. The light gray parts are undefined regions due to the lack of borehole information in the periphery of the deposit. Contours indicate topography.

Figure 4. Lithology and alteration models based on borehole data: (a) A cross-section of 3D lithology model along profile AA' in Figure 3 (5738800m N). (b) A cross-section of 3D alteration model along the same profile. The Newton Hill Fault (NHF) has disrupted the continuity of all lithological units and offsets the mineralized zone. The gold mineralization correlates strongly with quartz-sericite alteration, predominantly in the felsic volcanic unit.

Figure 5. Magnetic susceptibilities of drillcores on profile AA'. High magnetic mafic volcanic rocks and dioritic intrusions are separated from other low magnetic rocks (felsic volcanic rocks and porphyritic intrusions).

Figure 6. Boxplot demonstration of measured magnetic susceptibilities and γ-ray potassium (K) concentrations of different lithologies and alteration assemblages. Susceptibility axis is logarithmic.

Figure 7. Magnetic and DC/IP datasets. All data are draped on a shaded relief digital elevation model (DEM) of the region: (a) Airborne total magnetic field intensities (TF) on a regional scale (GSC database). (b) Helicopter-borne total magnetic field intensities (TF) on deposit scale (Amarc dataset) together with locations of DC/IP profiles.

Figure 8. Ternary images of airborne radiometric datasets (GSC): (a) Deposit scale RGB image of K-eTh-eU channels. White regions indicate the overlaps of all three elemental RGB channels. (b) Deposit scale RGB image of K/eTh-eTh/eU-eU/K channels.

Figure 9. Sharp regional MVI model after four IRI focused on the high and low magnetic susceptibility zones: (a) The 3D MVI susceptibility model on a plan view (draped on shaded relief topography). (b) The 3D MVI susceptibility model cross-cut on the profiles AA' 5738800m N. Directions of magnetization vectors are overlain on the cross-section AA'. Outlines of the hydrothermal zone and Newton deposit area are shown in the rectangles.

Figure 10. Deposit scale unconstrained MVI model after four IRI on Amarc datasets: (a) The 3D MVI susceptibility model on a plan view draped on shaded relief topography (Outline of Au-Ag-Cu mineralization is shown in the black contour). (b) The 3D MVI susceptibility model sliced at the elevations of 1000 m (the bedrock geology is overlapped). (c) The 3D MVI susceptibility model cross-cut on the profiles AA' at 5738800m N. Directions of magnetization vectors are overlain on the cross-section AA'.

Figure 11. Deposit scale inversion of DC/IP data over Newton deposit: (a) Plan view of the recovered resistivity model draped on a shaded relief topography model (Outline of Au-Ag-Cu mineralization is shown in the black contour). (b) Resistivity model sliced at elevation 1000 m (the bedrock geology is overlapped). (c) Resistivity model cross-cut on the profile AA' at 5738800m N (Outline of Au mineralization is shown in the black contour).

Figure 12. Deposit scale inversion of DC/IP data over Newton deposit: (a) Plan view of the recovered chargeability model draped on a shaded relief topography model (Outline of Au-

Ag-Cu mineralization is shown in the black contour). (b) Chargeability model sliced at elevation 1000 m (the bedrock geology is overlaid on the model). (c) Chargeability model cross-cut on the profile AA' at 5738800m N (Outline of Au mineralization is shown in the black contour).

Figure 13. Deposit scale cooperative magnetic-DC/IP inversions sliced at the elevation of 1000 m: (a) Electrical resistivity model. (b) IP chargeability model. (c) Magnetic susceptibility model. The bedrock geology is overlaid on all models. The gray shaded zone is the outline of Au-Ag-Cu mineralization.

Figure 14. Petrophysical domains inferred from the integration of cooperatively inverted physical properties on the three physical properties' cross-plots. (a) A susceptibility-resistivity cross-plot with two distinct domains related to the high and low chargeability values. (b) A susceptibility-chargeability cross-plot with two distinct domains related to the high and low resistivity values. (c) A resistivity-chargeability cross-plot with two distinct domains related to the high and low susceptibility values.

Figure 15. Results of cooperative modeling compared with borehole information cross-cut on the profile AA' at 5738800m N in Figure 3: (a) Electrical resistivity model. (b) IP chargeability model. (c) Magnetic susceptibility model. (d) Integrated geological interpretation.

LIST OF TABLES

Table 1. Classified petrophysical domains based on inverted physical properties and their integrated interpretation.

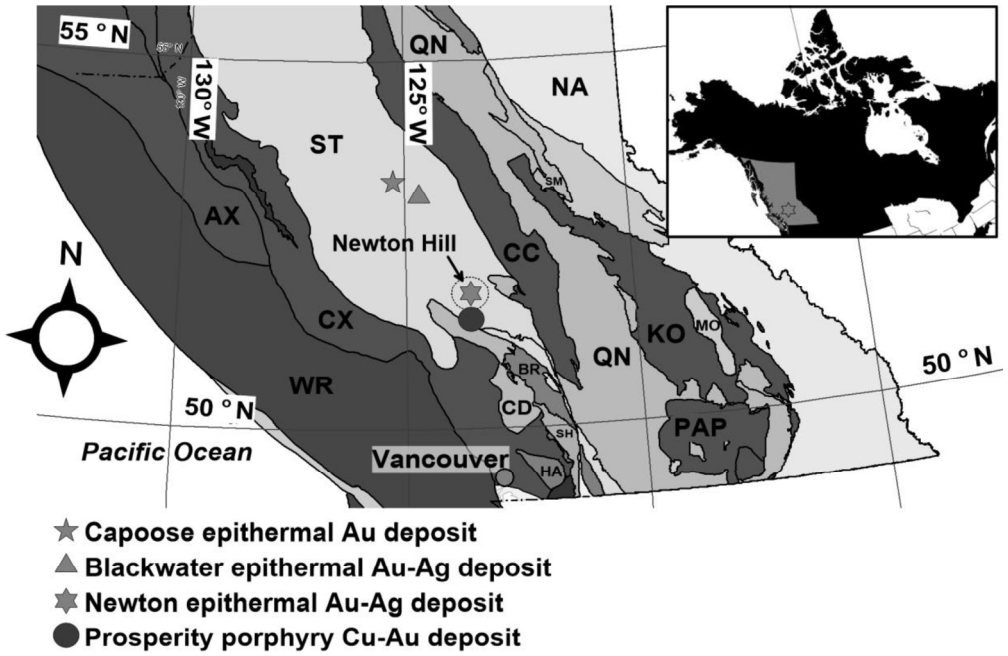

Figure 1. Several large porphyry and epithermal deposits located in Stikinia terrain (ST) in central British Columbia.

169x110mm (300 x 300 DPI)

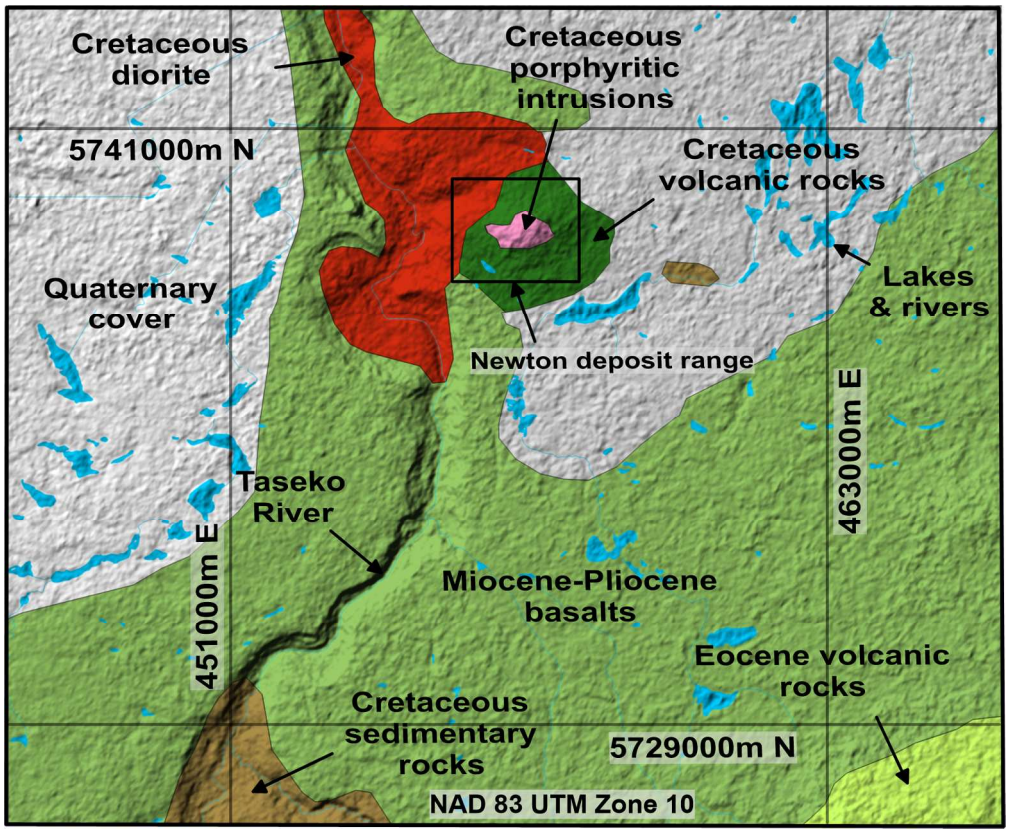

Figure 2. Regional geological features of Newton area.

169x139mm (300 x 300 DPI)

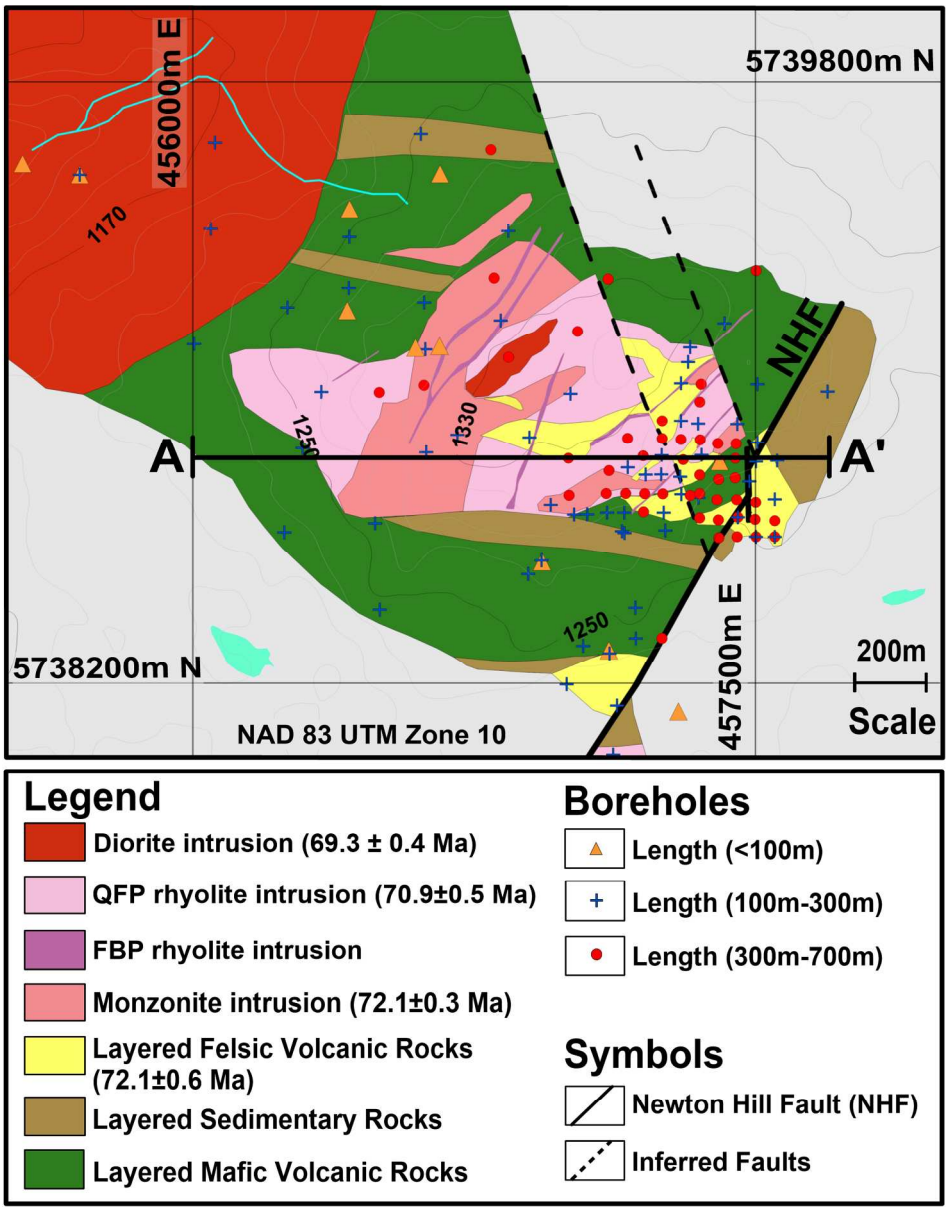

Figure 3. Bedrock geology map at the deposit scale

169x215mm (300 x 300 DPI)

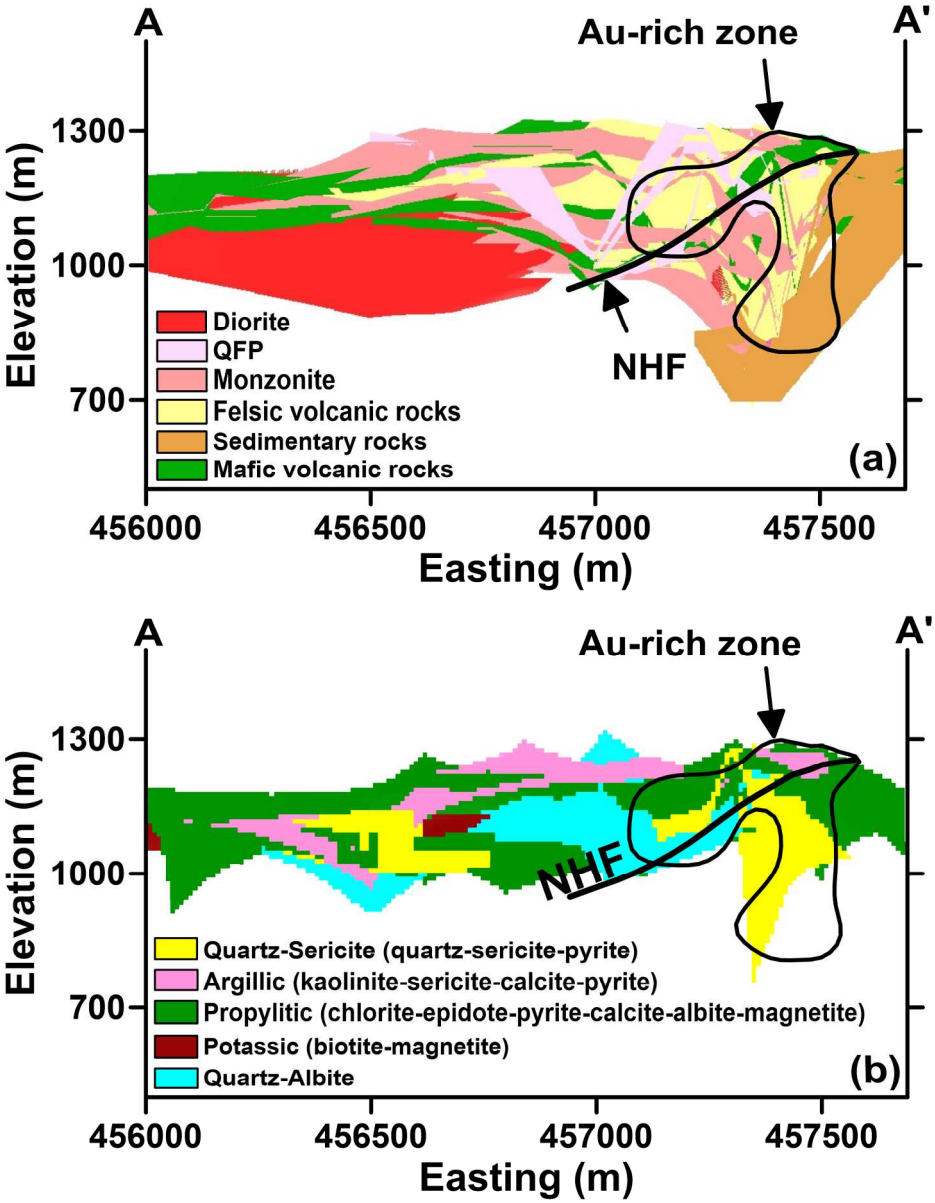

Figure 4. (a) A cross-section of 3D lithology model along profile AA' in Figure 3. (b) A cross-section of 3D alteration model along the same profile.

169x217mm (300 x 300 DPI)

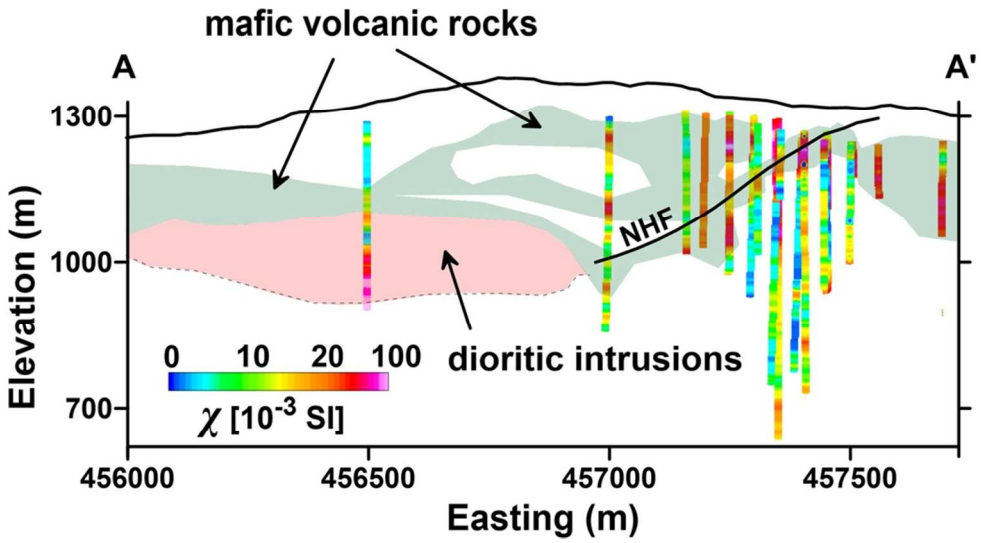

Figure 5. Magnetic susceptibilities of drillcores on profile AA'.

90x48mm (300 x 300 DPI)

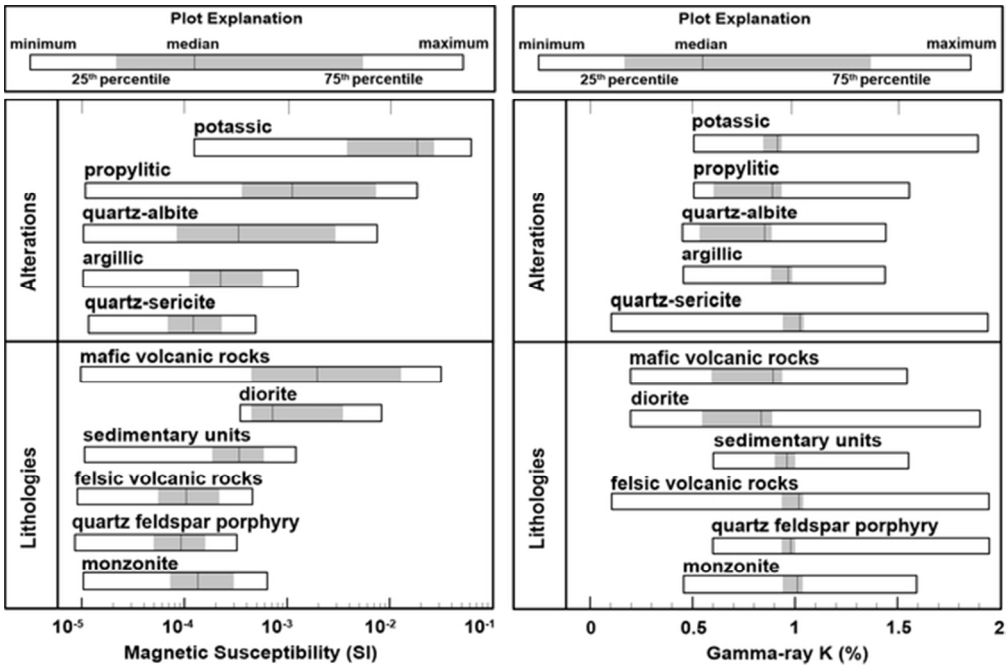

Figure 6. Boxplot demonstration of measured magnetic susceptibilities and γ-ray potassium (K) concentrations of different lithologies and alteration assemblages. Susceptibility axis is logarithmic.

55x36mm (300 x 300 DPI)

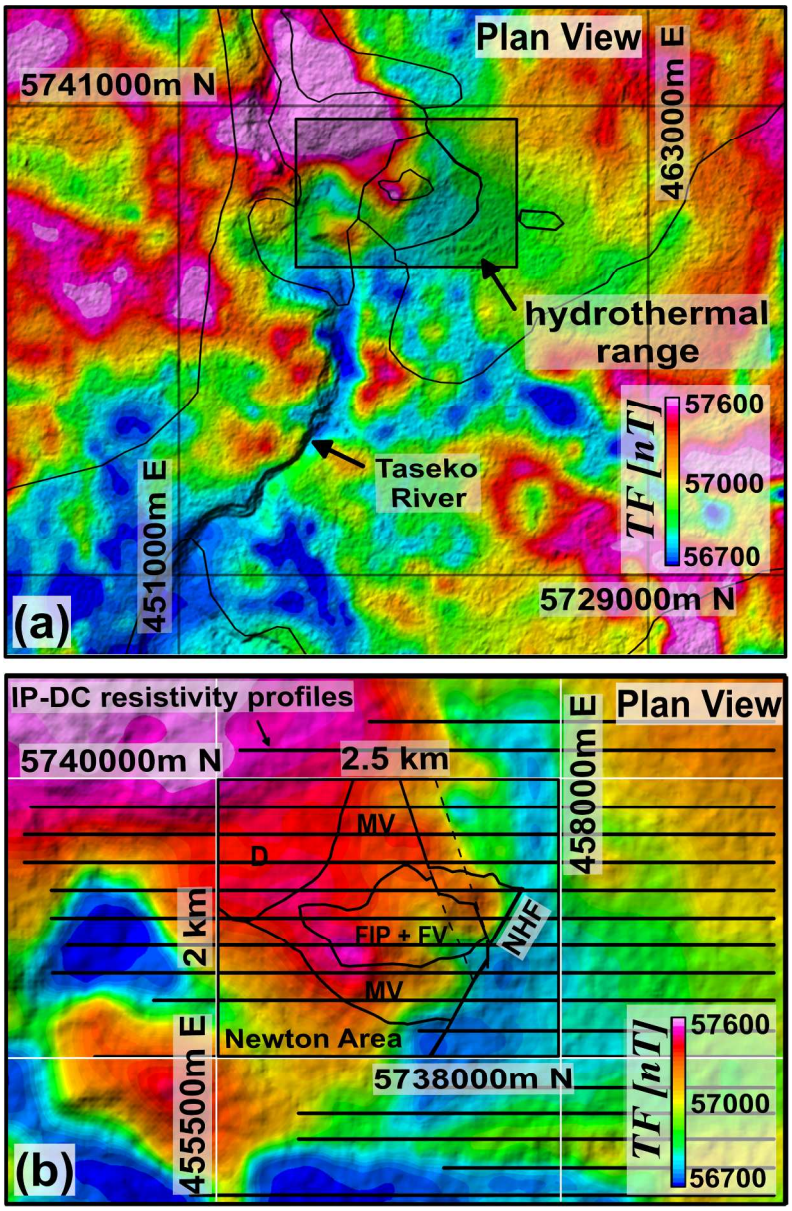

Figure 7. Magnetic and IP-DC-resistivity datasets. (a) Total magnetic field intensities on a regional scale. (b) Total magnetic field intensities on deposit scale together with locations of DC/IP profiles.

169x258mm (300 x 300 DPI)

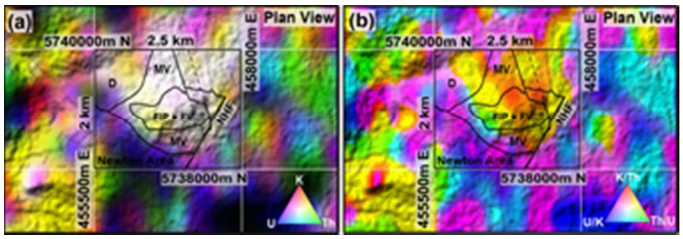

Figure 8. Ternary images of airborne radiometric datasets: (a) RGB image of K-eTh-eU channels. (b) RGB image of K/eTh-eTh/eU-eU/K channels.

28x9mm (300 x 300 DPI)

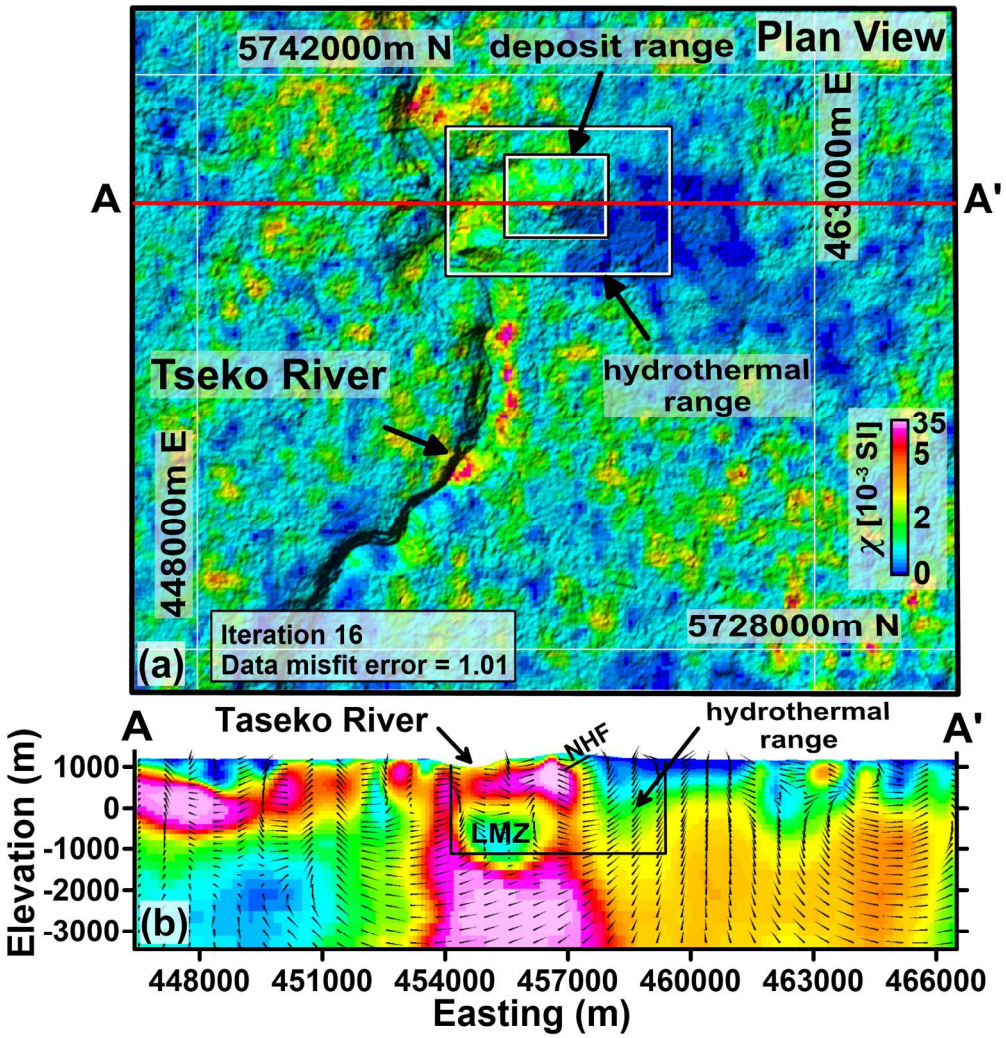

Figure 9. Sharp regional MVI model. (a) The MVI susceptibility model on a plan view. (b) The 3D MVI susceptibility model cross-cut on the profiles AA' 5738800m N.

169x173mm (300 x 300 DPI)

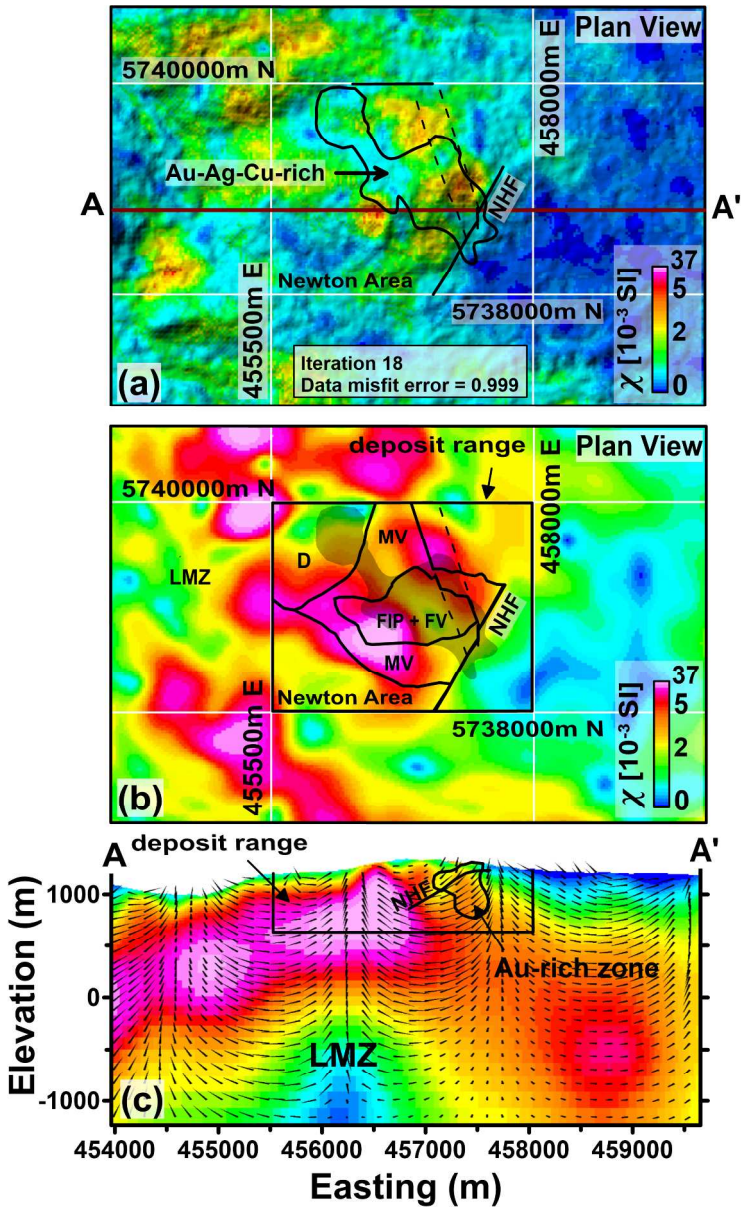

Figure 10. Deposit scale unconstrained MVI model. (a) The susceptibility model on a plan view. (b) The susceptibility model sliced at the elevations of 1000 m. (c) The susceptibility model cross-cut on the profiles AA' at 5738800m N.

169x274mm (300 x 300 DPI)

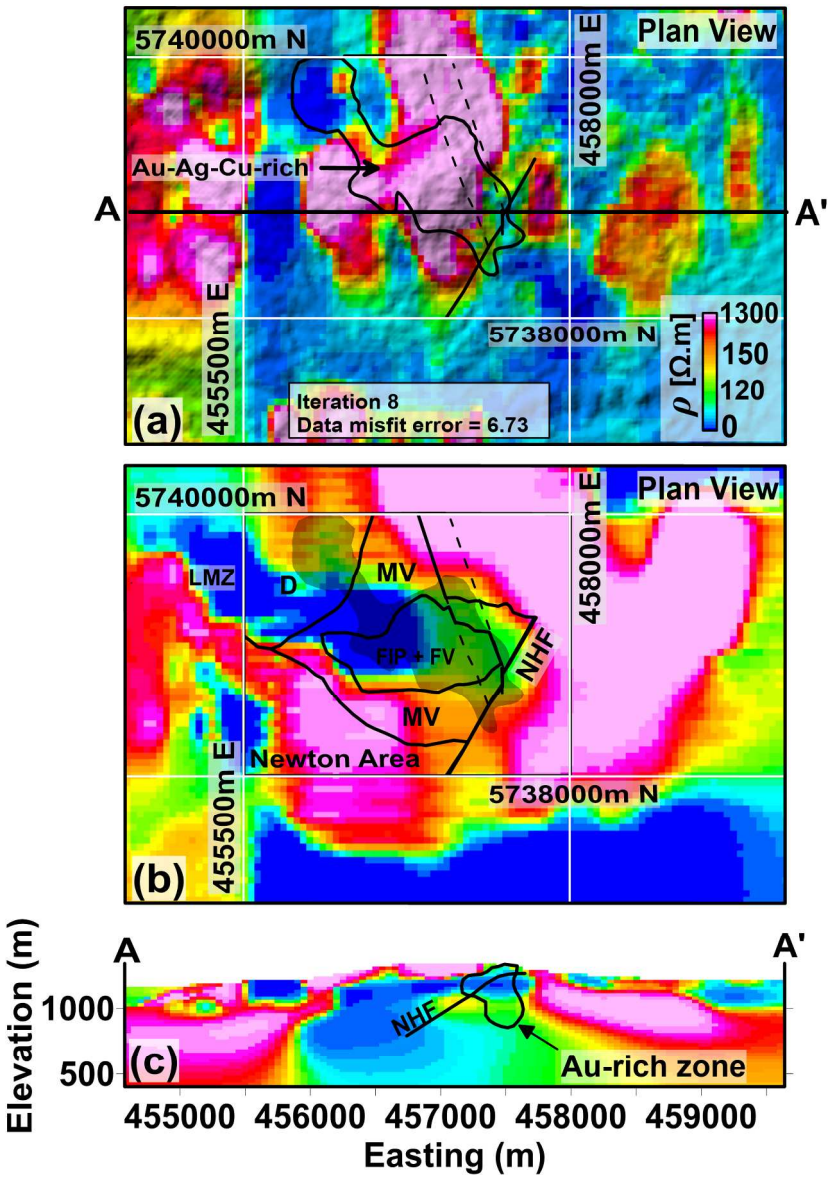

Figure 11. Deposit scale inversion of DC/IP data: Recovered resistivity model. (a) Plan view of the resistivity model. (b) Resistivity model sliced at elevation 1000 m. (c) Resistivity model cross-cut on the profile AA' at 5738800m N.

169x245mm (300 x 300 DPI)

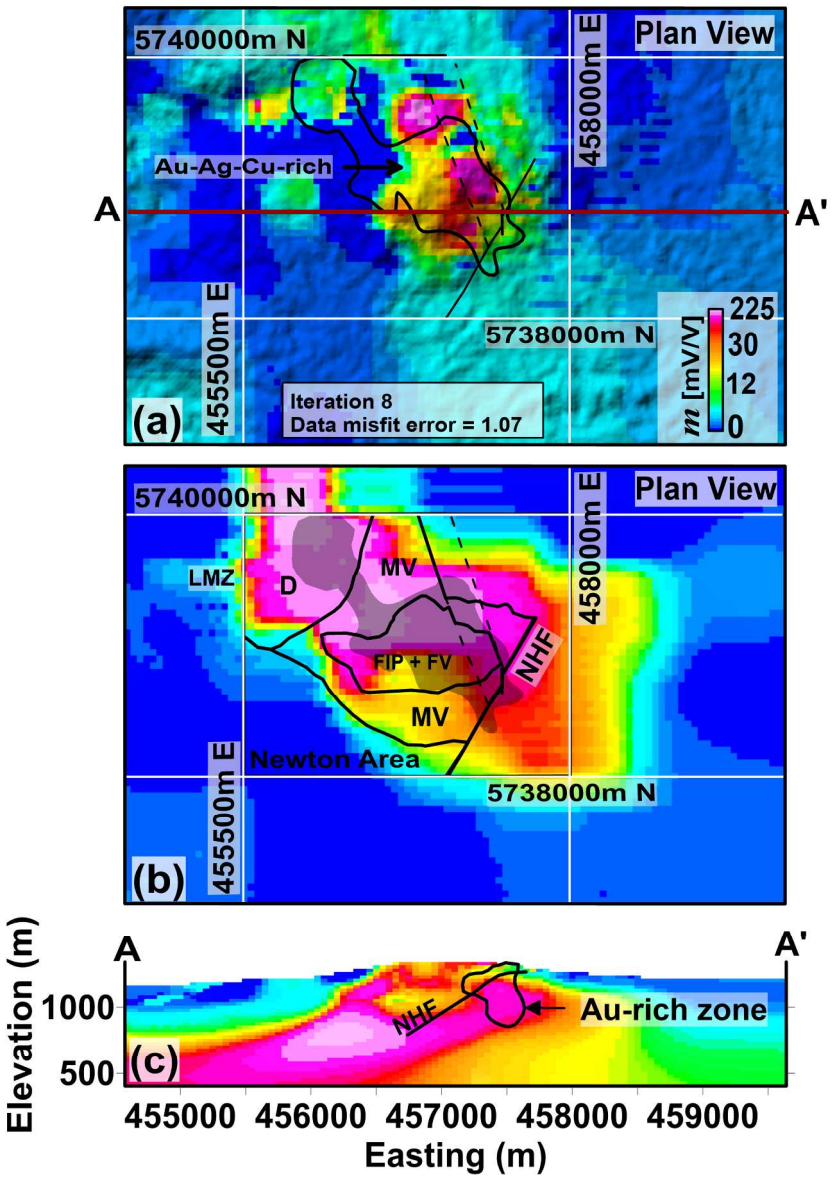

Figure 12. Deposit scale inversion of DC/IP: (a) Plan view of the chargeability model. (b) Chargeability model sliced at elevation 1000 m. (c) Chargeability model cross-cut on the profile AA' at 5738800m N.

169x245mm (300 x 300 DPI)

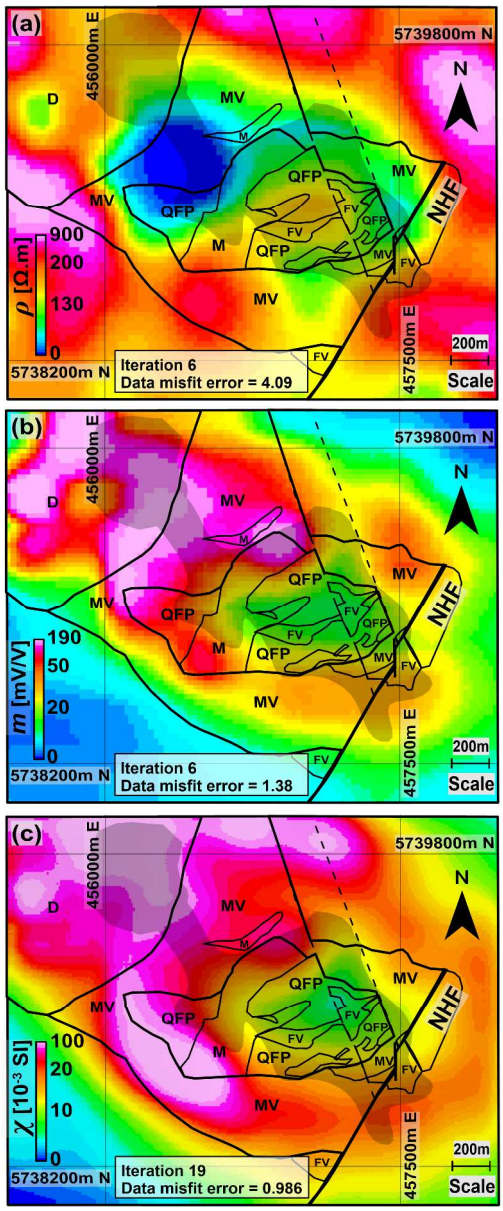

Figure 13. Deposit scale cooperative magnetic-DC/IP inversions sliced at the elevation of 1000 m: (a) Resistivity model. (b) Chargeability model. (c) Susceptibility model.

169x399mm (300 x 300 DPI)

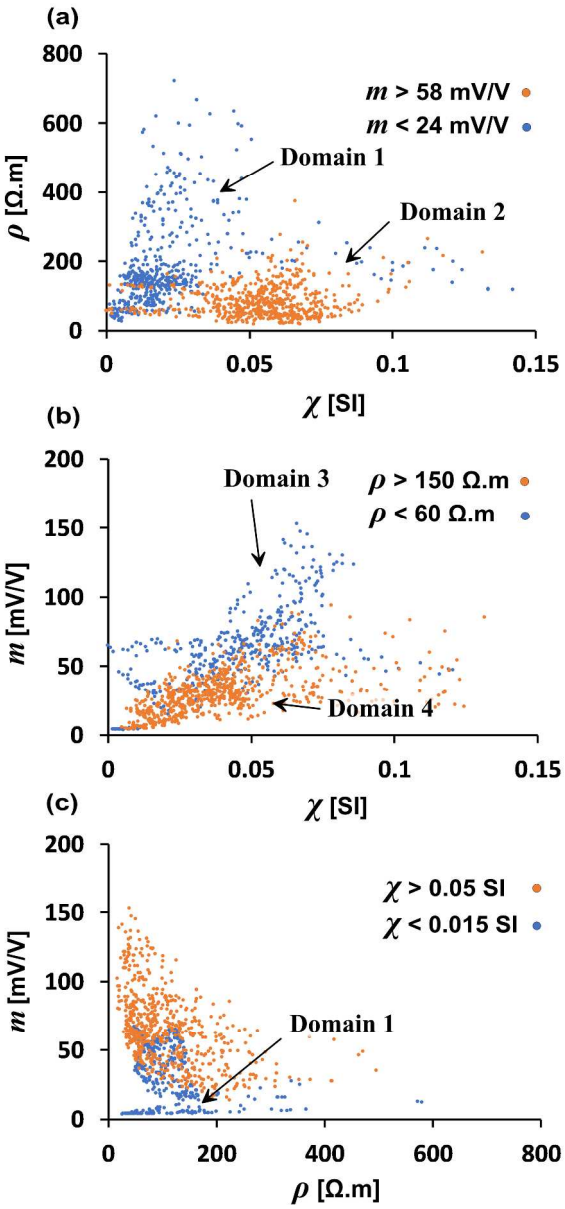

Figure 14. Petrophysical domains inferred from the integration of cooperatively inverted physical properties on the three physical properties' cross-plots. (a) A susceptibility-resistivity cross-plot. (b) A susceptibility-chargeability cross-plot. (c) A resistivity-chargeability cross-plot.

169x351mm (300 x 300 DPI)

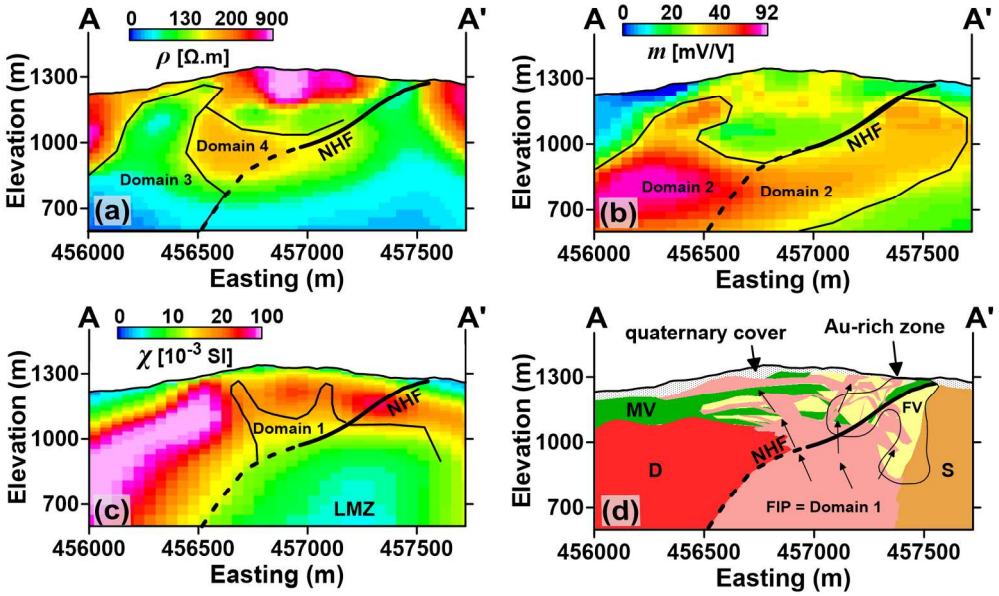

Figure 15. Results of cooperative modeling compared with borehole information. (a) Resistivity model. (b) Chargeability model. (c) Susceptibility model. (d) Integrated geological interpretation.

169x100mm (300 x 300 DPI)

Table 1. Classified petrophysical domains based on inverted physical properties and their integrated interpretation.

Domain	ρ [Ω.m]	m [mV/V]	χ [10^{-3} SI]	Interpretation
1	No signature	Low	Low	Porphyritic intrusions in the center.
2	Low	High	No signature	Sulfide dissemination (periphery of the Au-rich zone)
3	Low	High	High	Cu-rich (north-west of the Newton Hill)
4	High	Low	Low	Au-Ag-Cu-rich with silicifications in the center.

DATA AND MATERIALS AVAILABILITY

Data associated with this research are confidential and cannot be released.